

Article

Preparation of Mn-Co-MCM-41 Molecular Sieve with Thermosensitive Template and Its Degradation Performance for Rhodamine B

Wenju Peng ¹, Lixia Cai ^{2,*}, Yani Lu ¹ and Yaoyao Zhang ^{3,*}

¹ School of Civil Engineering, Hubei Engineering University, Xiaogan 432000, China; pwj1112@foxmail.com (W.P.)

² College of Technology, Hubei Engineering University, Xiaogan 432000, China

³ School of Chemistry and Materials Science, Hubei Engineering University, Xiaogan 432000, China

* Correspondence: cailixia@hbeu.edu.cn (L.C.); yaoyaozhang@hbeu.edu.cn (Y.Z.)

Abstract: Rhodamine B (RhB) in dyes is widely used in various industries, but it poses a great threat to the natural environment and human health. In this work, a series of thermosensitive polymer materials, PN_xD_y , with controllable morphology and particle size were prepared by free radical polymerization using *N*-isopropylacrylamide and *N,N*-dimethylacrylamide as monomers. Then, by using PN_xD_y as a template, bimetallic Mn- and Co-doped MCM-41 molecular sieves with good morphology and properties were prepared by the microwave-assisted hydrothermal method. The effects of a series of thermosensitive templates on the morphology and properties of the Mn-Co-MCM-41 molecular sieve were investigated. The results demonstrated that the Mn-Co-MCM-41 by $PN_{100}D_4$ as a templating agent showed the best mesoporous ordering and the most regular material morphology with 2 nm nanoparticles. In addition, the molecular sieve with the best structure was selected for the RhB degradation experiments. The Mn-Co-MCM-41 with $PN_{100}D_4$ as the template showed regular morphology and uniform pore channels. It was applied as a catalyst for the degradation of RhB by potassium monopersulfate (PMS). The degradation rate of RhB could reach 98% with a 20 min reaction by Mn-Co-MCM-41 ($PN_{100}D_4$). Meanwhile, the degradation rate could be maintained at 91% after being reused six times. The bimetallic-doped Mn-Co-MCM-41 molecular sieves prepared using the thermosensitive material $PN_{100}D_4$ as a template have good catalytic performance and can be effectively reused.

Keywords: thermosensitive polymer; Mn-Co bimetallic; MCM-41 molecular sieve; rhodamine B; recycle



Citation: Peng, W.; Cai, L.; Lu, Y.; Zhang, Y. Preparation of Mn-Co-MCM-41 Molecular Sieve with Thermosensitive Template and Its Degradation Performance for Rhodamine B. *Catalysts* **2023**, *13*, 991. <https://doi.org/10.3390/catal13060991>

Academic Editors: Jiangkun Du, Lie Yang and Chengdu Qi

Received: 10 May 2023

Revised: 5 June 2023

Accepted: 7 June 2023

Published: 9 June 2023



Copyright: © 2023 by the authors. Licensee MDPI, Basel, Switzerland. This article is an open access article distributed under the terms and conditions of the Creative Commons Attribution (CC BY) license (<https://creativecommons.org/licenses/by/4.0/>).

1. Introduction

With the development of the industrial revolution, dyes have been widely used in the food, pharmaceutical, printing, and cosmetic industries. However, dyes also cause environmental pollution, such as water pollution, dramatically threatening human health [1,2]. Rhodamine B (RhB) is a common organic pollutant that is difficult to degrade and accumulates quickly, causing cancer, and has a long half-life [3–5]. Several methods have been used to degrade RhB [6–8]. Until now, photocatalytic decay of pollutants has been widely studied [9], but dyes are quite stable to radiation, and oxidation and the presence of intermediates make water unsuitable for drinking [10]. Catalytic oxidation, the most used chemical process, has the benefits of non-toxicity, safety, stability, and high catalytic activity [11]. The catalysts used for RhB degradation are carbon-based materials [12], zinc-based materials [13], and molecular sieve titanium-based materials [14]. However, there are disadvantages to the current catalysts, including an inadequate catalytic effect and challenging catalyst reuse.

Since the 1960s, molecular sieves such as MCM-41 molecular sieves [15,16], 4A molecular sieves [17], and SBA-15 molecular sieves [18] have been widely used in separation

processes, object chemistry, gas sensors, drug delivery, and optoelectronic devices due to their unique structures and superior properties. MCM-41 molecular sieves are more conducive to the rapid diffusion of organic molecules due to their uniform pore size, large specific surface area, and higher adsorption capacity than other pore channel materials. Therefore, they can be utilized as catalysts or adsorbents [19–21]. However, the weak acidity of pure silicon MCM-41 molecular sieves and the homogeneity of the silicon skeleton structure severely limit the application of MCM-41. In particular, the lack of active centers in the pore walls limits its application in catalysis [22–25]. Subsequent studies have mainly used the introduction of heteroatoms such as Cu, Fe, Sr, Ti, Zn, and V [21,26]. Pradhan et al. [27] used oleic acid and cetyltrimethylammonium bromide (CTAB) as particle size controllers (capping agents) and morphology controllers (surfactant). In the framework structure of mesoporous Al₂O₃-MCM-41, Co-Fe, Mn-Co, and Fe-Mn bimetallic nanoparticles were prepared. In this system, photo-Fenton and photocatalytic processes effectively degraded the dyes, with 100% degradation within 60 min. However, the metals were highly prone to agglomeration during the doping process [17,28]. They would result in inhomogeneous doping, irregular molecular sieve structure, unstable catalyst activity, and limited catalytic performance. The use of the template is crucial in the preparation method of regularly shaped MCM-41 materials. Thermosensitive materials, as new materials, can achieve structural diversity by controlling the morphology of reactive monomers and have a wide range of applications in templating agents.

In this study, self-prepared thermosensitive nanoparticles were used as templates. In situ filling of manganese (Mn) and cobalt (Co) salts into the pores of molecular sieve MCM-41 took place using the microwave-assisted hydrothermal method. Thus, bimetallic Mn-Co-doped MCM-41 molecular sieve materials with good morphology and properties were prepared, and Co²⁺/Co³⁺, Mn²⁺/Mn³⁺, and Mn³⁺/Mn⁴⁺ redox pairs could dominate the activation of potassium monopersulfate (PMS) to degrade Rhodamine-B dye [29]. The effects of the doping amounts of bimetallic Mn and Co on the morphology and properties of the MCM-41 molecular sieve were systematically investigated. In addition, the best-structured molecular sieve was screened and applied as a catalyst for the degradation of RhB by PMS. The bimetallic doped MCM-41 catalyst prepared in this work provides a new method for the industrial degradation of RhB.

2. Materials and Methods

2.1. Experimental Reagents and Instruments

Main reagents: N-isopropylacrylamide, *N,N*-dimethylacrylamide, azodiisobutyronitrile, mercaptoethylamine hydrochloride, ethyl orthosilicate, manganese nitrate, cobalt nitrate, methanol, tetrahydrofuran, PMS, RhB, and deionized water.

Main instruments: an electronic balance, a hydrothermal reactor, a Schlenk reaction tube, a vacuum drying oven, a microwave reactor, an ultrasonic cleaner, a tube furnace, a scanning electron microscope, an elemental analyzer, a UV-Vis spectrophotometer, an infrared spectrometer, and a specific surface area analyzer.

2.2. Synthesis of the Thermosensitive Template PN_xD_y

Based on the free radical polymerization method, *x* mmol of N-isopropylacrylamide and *y* mmol of *N,N*-dimethylacrylamide were added as reaction monomers to the Schlenk reaction tube. Azo diisobutyronitrile was used as the chain initiator, mercaptoethylamine hydrochloride was used as the chain transfer agent, and methanol was used as the reaction solvent. The reaction was carried out in an oil bath at 60 °C for 24 h. The solvent was removed at the end of the reaction. The solid product was precipitated with ether and dried under vacuum at 30 °C to obtain the thermosensitive polymer PN_xD_y. *x* and *y* denote the degree of polymerization of N-isopropylacrylamide and *N,N*-dimethylacrylamide, respectively. Three thermosensitive polymers with different hydrophilic ratios were prepared, and their characterization results are shown in Table 1 [30].

Table 1. Characterization of three polymers with different hydrophobic ratios.

Polymers	Hydrophilic/Hydrophobic Ratio	GPC	LCST(°C)	Morphology	Particle Size
PN ₁₂₀ D ₄	30:1	17,624	34.0	Random	/
PN ₁₀₀ D ₄	25:1	16,121	33.5	Nanoparticles	2 nm
PN ₈₀ D ₄	20:1	14,573	33.0	Nanoparticles	3 nm

GPC: Gel permeation chromatography; LCST: lowest critical solution temperature.

2.3. Preparation of the Bimetallic (Mn-Co)-Doped MCM-41 Molecular Sieve with PN_xD_y

Approximately 1 g of PN_xD_y was dissolved in 100 mL of water and stirred by microwave at 20 °C for 30 min. Approximately 9 mL of ammonia was added to adjust the pH to 11. Magnetic stirring was continued for 30 min. Approximately 50 mmol of ethyl orthosilicate, 1 mmol of manganese nitrate, and 1 mmol of cobalt nitrate were added to the solution, and it was placed in a high-pressure hydrothermal reactor at 140 °C for 10 h to maintain Si:Mn:Co = 50:1:1. Then, when it cooled to room temperature, the sample was removed by centrifugation and dried under vacuum at 50 °C. The bimetallic (Mn-Co)-doped MCM-41 molecular sieve precursors were obtained by grinding to powder. The powder was roasted in the N₂ atmosphere in a tube furnace to obtain the final product of the bimetallic (Mn-Co)-doped MCM-41 molecular sieve (named Mn-Co-MCM-41(PN_xD_y)). The roasting parameters were: 2 °C/min, 1 h at 100 °C, and 3 h at 500 °C [31].

2.4. Characterization of the Molecular Sieve

The PN_xD_y, Mn-Co-MCM-41 molecular sieve, and Mn-Co-MCM-41(PN_xD_y) were characterized. Fourier transform infrared spectroscopy (FTIR) was performed using a Vertex 70 FTIR spectrometer (Germany). Sample composition was determined by characteristic peak analysis. The scan number was 32. The scanning range was 400–4000 cm⁻¹ with a 0.1–16 cm⁻¹ resolution. Ultraviolet–visible spectroscopy (UV-Vis) measurements were performed using an ultraviolet spectrometer (Agilent 8453 type) with a 200–900 nm wavelength range. Nuclear magnetic resonance (NMR) characterization of polymers was performed using a Bruker Drx 400 instrument (Bruker Company, Bremen, Germany) with D₂O as solvent. The molecular weight of the polymers was measured by gel chromatography (Alltech Instrument Company, Lexington, KY, USA) using tetrahydrofuran as the mobile phase solvent. Transmission electron microscopy (TEM, Tecnai F20) was used to characterize the morphology of the polymer in water and the particle size. The test voltage was 200 kV. The morphology of the Mn-Co-MCM-41 prepared under different template agents was characterized by scanning electron microscopy (SEM, JSM-6510). The X-ray diffraction (XRD) spectra of the samples were collected using an X-ray diffractometer (X'pert MPD Pro, Philips Company, Amsterdam, The Netherlands). A specific surface area analyzer (BSD-660M A6M) was used to determine the specific surface area of the samples.

2.5. Degradation Performance of RhB by the Molecular Sieve

The 5 mg/L RhB solution was prepared, and 60 mL of RhB solution was added to a 100 mL conical flask. Approximately 5 mg (Co amount is 0.5% of Rhodamine-B dye) Mn-Co-MCM-41(PN_xD_y) was weighed and then mixed into it. Different concentrations of PMS solution (0, 0.1 mmol/L, 0.2 mmol/L, and 0.3 mmol/L) were added and shaken well and then magnetically stirred. Approximately 1 mL samples were taken at 2 min intervals. The reaction was filtered through a 0.22 μL membrane and terminated by adding 100 μL of anhydrous ethanol. The remaining RhB in the solution was then measured using the UV spectrophotometer to determine the degradation rate at each time point [32].

3. Results and Discussion

3.1. Characterization of the Thermosensitive Polymer PN₁₀₀D₄

The FTIR and lowest critical solution temperature (LCST) characterizations of the prepared thermosensitive polymer PN_xD_y are shown in Figures 1 and 2, respectively.

The characteristic peaks of the thermosensitive polymer PN_xD_y were at 3310 cm^{-1} and 3074 cm^{-1} , attributed to -NH- in -CONH- ; at 2975 cm^{-1} and 2932 cm^{-1} , attributed to -CH- in -CH-CH- ; at 2876 cm^{-1} , attributed to -CH_3 in $\text{-CH(CH}_3)_2$; and at 1653 cm^{-1} and 1540 cm^{-1} , attributed to -CH- in $\text{-CH(CH}_3)_2$ (as shown in Figure 1).

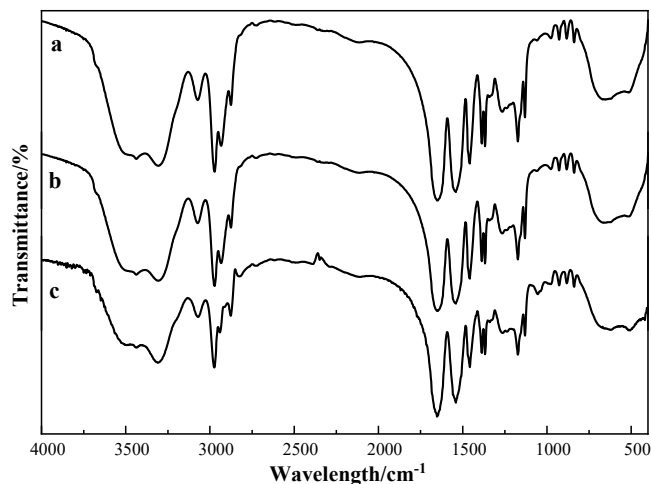


Figure 1. Infrared spectrum of $\text{PN}_{120}\text{D}_4$ (a), $\text{PN}_{100}\text{D}_4$ (b), and PN_{80}D_4 (c).

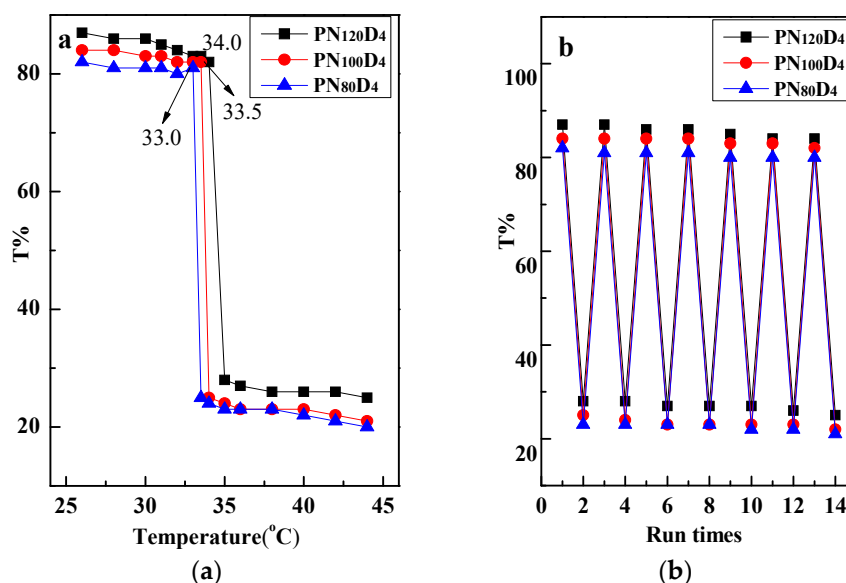


Figure 2. Testing of PN_xD_y : (a) LCST; (b) temperature responsiveness test.

The thermosensitive polymer PN_xD_y was configured into 0.5 mmol/L aqueous solution. The LCST test was performed by UV characterization, and the absorbance values at $\lambda_{\text{max}} = 450\text{ nm}$ were measured (as shown in Figure 2a). The transmittance of $\text{PN}_{100}\text{D}_4$ decreased abruptly at $33.5\text{ }^\circ\text{C}$. The solution was clear and transparent below $33.5\text{ }^\circ\text{C}$ and then became turbid when it increased above $33.5\text{ }^\circ\text{C}$. The LCST of polymer $\text{PN}_{120}\text{D}_4$ was $34.0\text{ }^\circ\text{C}$ and polymer PN_{80}D_4 was $33.0\text{ }^\circ\text{C}$. It was repeatedly ramped up and down for the temperature response tests (Figure 2b). The results showed that $\text{PN}_{100}\text{D}_4$ dissolved at low temperatures and precipitated from the aqueous phase after ramping up, indicating that the thermosensitive polymer $\text{PN}_{100}\text{D}_4$ has excellent temperature response performance.

Transmission electron microscopy (TEM) and dynamic light scattering (DLS) characterization of $\text{PN}_{100}\text{D}_4$ were performed. The results are shown in Figure 3. The catalyst was configured in 0.5 mmol/L aqueous solution, and the samples were prepared and characterized by TEM. In Figure 3a–c, with the TEM of $\text{PN}_{120}\text{D}_4$ (a), $\text{PN}_{100}\text{D}_4$ (b), and

PN₈₀D₄ (c), the images show that PN₁₀₀D₄ has formed homogeneous nanoparticles with a diameter of about 2 nm, and PN₈₀D₄ showed nanoparticles with a diameter of about 3 nm. Figure 3d is the dynamic light scattering (DLS) of PN₁₂₀D₄, PN₁₀₀D₄, and PN₈₀D₄. The hydration kinetic particle size D_H of PN₁₀₀D₄ was 39.5 nm, and the PDI value was only 0.227, indicating that the polymer formed a homogeneous spherical structure, while PN₈₀D₄ showed a larger D_H of 91.3 nm with 0.382 PDI. The comprehensive analysis showed that the polymer could form nanoparticles with regular shapes and uniform size in water, which can be used as an excellent templating agent to prepare bimetal-doped MCM-41 materials.

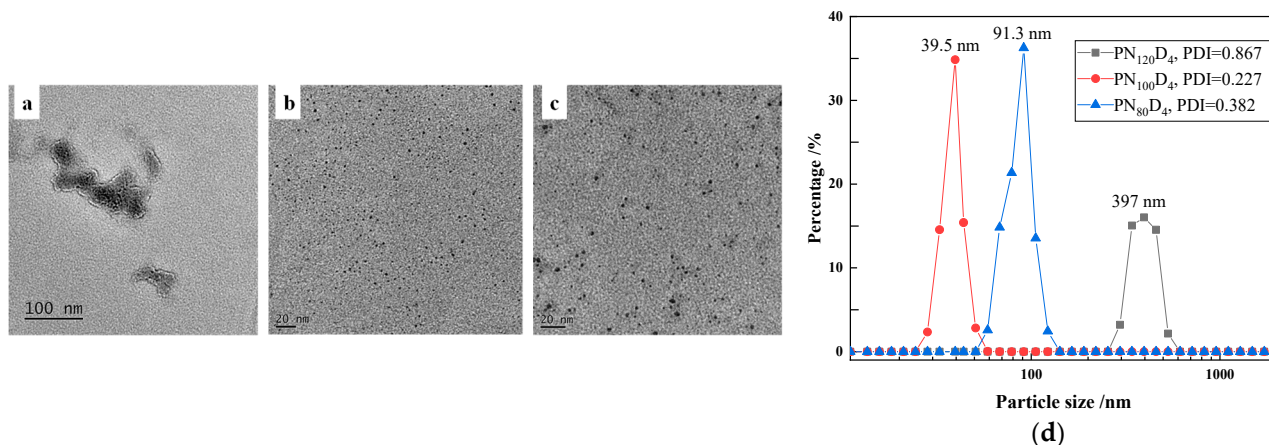


Figure 3. TEM of PN₁₂₀D₄ (a), PN₁₀₀D₄ (b), and PN₈₀D₄ (c). (d) Dynamic light scattering (DLS).

3.2. Characterization of the Bimetallic Mn-Co Doped MCM-41 Molecular Sieve

3.2.1. FTIR

The FTIR test results of Mn-Co-MCM-41 are shown in Figure 4.

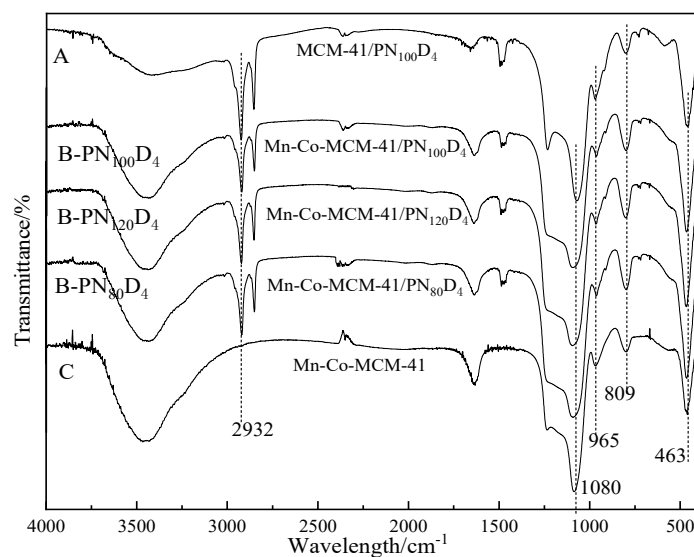


Figure 4. Infrared spectra of the MCM-41(PN₁₀₀D₄) and Mn-Co-MCM-41(PN_xD_y) molecular sieves.

Curve A is the FTIR spectrum of MCM-41/PN₁₀₀D₄ with unloaded metal. Its characteristic peaks correspond to the 1080 cm⁻¹ peak being attributed to the asymmetric stretching vibration of the Si-O tetrahedra; the 965 cm⁻¹ peak being attributed to the stretching vibration of the Si-O bond; the 809 cm⁻¹ peak being attributed to the symmetric stretching vibration of the Si-O tetrahedra; and the 463 cm⁻¹ peak being attributed to the bending vibration of the Si-O bond. The comprehensive analysis showed that MCM-41 had a unique skeleton of molecular sieves.

Curve B is the FTIR spectrum of MCM-41 after metal loading. Characteristic peaks of thermosensitive materials appeared in both B and A at 2932 cm^{-1} due to the use of the templating agent. Curve B is similar to curve A, indicating that Mn-Co doping did not destroy the skeletal structure of MCM-41. Curves B-PN₁₀₀D₄, B-PN₁₂₀D₄, and B-PN₈₀D₄ exhibited similar infrared characteristic peaks. The adsorption of the molecular sieve after doping with Mn-Co was stronger than that of pure silicon MCM-41. The absorption peak of Mn-Co-MCM-41(PN_xD_y) at $3400\sim 3800\text{ cm}^{-1}$ was stronger than that of the pure silicon MCM-41 molecular sieve. With Mn-Co doping, the characteristic peak near 965 cm^{-1} was enhanced because the introduction of the metal increased the asymmetry of the molecular sieve skeleton structure. It was indirectly proven that manganese and cobalt ions had penetrated the molecular sieve skeleton [33].

Curve C is the FTIR spectrum of Mn-Co-MCM-41(PN_xD_y) after calcination in the N₂ atmosphere. Compared with curve B, the uncalcined Mn-Co-MCM-41(PN_xD_y) had three peaks at 2920 cm^{-1} , 2850 cm^{-1} , and 1650 cm^{-1} , which were attributed to the characteristic peaks of the templating agent contained before calcination. After calcination, the disappearance of the three peaks proved that the thermosensitive template agent was completely removed. The other characteristic peaks of curve C were consistent with curve B, indicating that calcination did not destroy the pore structure of Mn-Co-MCM-41 [34].

3.2.2. Small-Angle XRD

Figure 5 shows the small-angle XRD spectra of Mn-Co-MCM-41(PN_xD_y) prepared from different thermosensitive polymers as surfactants. All samples showed distinct characteristic diffraction peaks around $2\theta = 2.2^\circ$, attributed to the (100) crystal plane in the two-dimensional hexagonal material structure. Without the templating agent, the characteristic peak of Mn-Co-MCM-41 was not obvious, and there was no sharp (100) crystallographic plane. With the addition of PN_xD_y, the characteristic peaks of the molecular sieve gradually appeared, and the characteristic peaks intensity of the (100) crystallographic plane increased. When the hydrophilic ratio of the polymer was at the maximum, the characteristic peak intensity of the two-dimensional hexagonal (110) crystallographic plane was enhanced under the action of PN₁₂₀D₄ compared to the one without the template. With the increasing hydrophobic ratio, the (100) crystallographic plane of the Mn-Co-MCM-41 structure formed by PN₁₀₀D₄ was the strongest. New characteristic peaks corresponding to the (110) and (200) crystallographic planes appeared at 4.0° and 4.7° , respectively. This demonstrated that the Mn-Co-MCM-41 had good mesoporous ordering and the most regular material morphology when using PN₁₀₀D₄ as a templating agent.

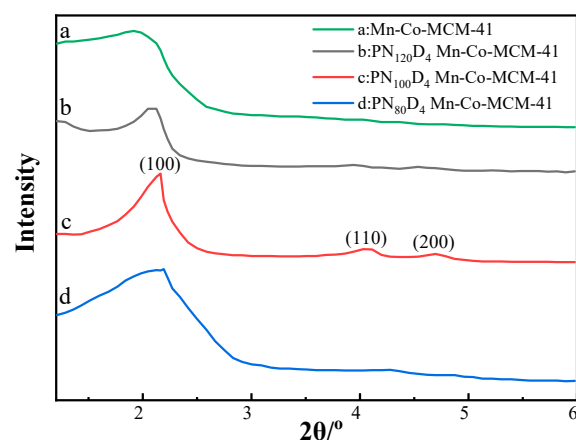


Figure 5. Small-angle XRD characterization of Mn-Co-MCM-41.

With the increasing hydrophobicity, the characteristic peak intensity of the two-dimensional hexagonal (110) crystal plane was significantly reduced under the action

of PN_{80}D_4 . Meanwhile, the characteristic peaks attributed to (110) and (200) disappeared, and the orderliness of the Mn-Co-MCM-41 material was reduced.

3.2.3. SEM

SEM characterization was performed to investigate the effect of the thermosensitive templating agent PN_xD_y on the morphology of Mn-Co-MCM-41. Figure 6a shows the Mn-Co-MCM-41 prepared without the addition of a thermosensitive templating agent. The Mn-Co-MCM-41 samples showed a random state with uneven dimensions when the thermosensitive templating agent was not added. After adding the templating agent, Mn-Co-MCM-41(PN_xD_y) (Figure 6b–d) had a more regular shape and started to appear cubic. Among them, when $\text{PN}_{120}\text{D}_4$ and PN_{80}D_4 were added, the samples both contained a few uniform spherical particles under the action of the templating agent. However, most of them showed irregular states. After adding $\text{PN}_{100}\text{D}_4$, Mn-Co-MCM-41($\text{PN}_{100}\text{D}_4$) showed a regular shape, and the cubic-shaped molecular sieve had a large specific surface area and a uniform size (Figure 6d). Therefore, the addition of the $\text{PN}_{100}\text{D}_4$ template agent was beneficial to the formation of regular morphology. The EDS elemental scan of the sample in Figure 7 showed that Mn and Co elements were successfully doped into the molecular sieve MCM-41, and the weight ratio Si:Mn:Co in Mn-Co-MCM-41($\text{PN}_{100}\text{D}_4$) was 50:1:1.

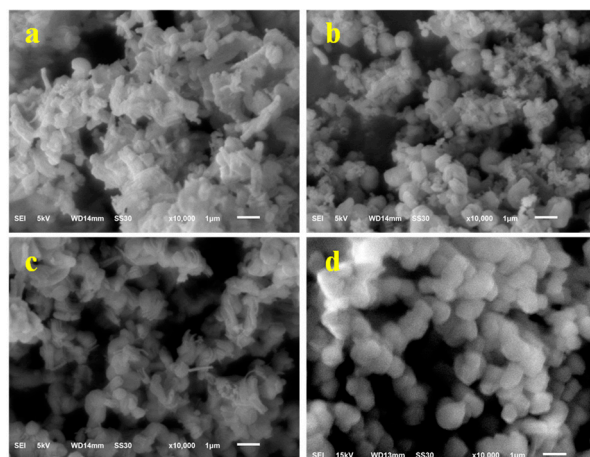


Figure 6. SEM of Mn-Co-MCM-41: (a) Mn-Co-MCM-41 prepared without a thermosensitive template; (b) Mn-Co-MCM-41 prepared with $\text{PN}_{120}\text{D}_4$; (c) Mn-Co-MCM-41 prepared with PN_{80}D_4 ; and (d) Mn-Co-MCM-41 prepared with $\text{PN}_{100}\text{D}_4$.

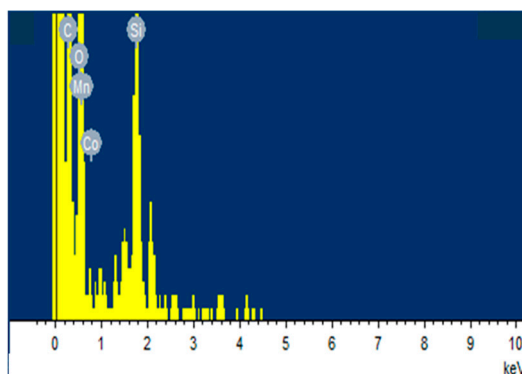


Figure 7. EDS of Mn-Co-MCM-41 prepared with $\text{PN}_{100}\text{D}_4$.

3.2.4. N_2 Adsorption–Desorption

The N_2 adsorption–desorption isotherm test results of Mn-Co-MCM-41 prepared with the $\text{PN}_{100}\text{D}_4$ thermosensitive material as a templating agent are shown in Figure 8. Mn-Co-MCM-41($\text{PN}_{100}\text{D}_4$) exhibited a type IV adsorption isotherm, indicating that the sample had

a typical and uniform structure. The adsorption amount increased rapidly in the interval of relative pressure from 0.2 to 0.4, indicating the uniform pore size distribution of the sample. In addition, there was no obvious hysteresis loop in the graph, indicating that the obtained Mn-Co-MCM-41(PN₁₀₀D₄) had a good pore structure when the PN₁₀₀D₄ thermosensitive material was used as the templating agent.

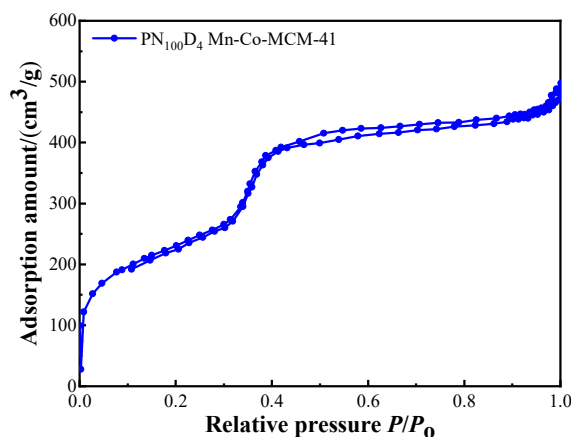


Figure 8. N₂ adsorption–desorption isotherm of Mn-Co-MCM-41 prepared with PN₁₀₀D₄.

3.3. Performance of Catalyst-Activated PMS for RhB Degradation

3.3.1. Influence of Catalyst Type

A comparative reaction test was used to investigate the effect of different thermosensitive templating agents on the efficiency of Mn-Co-MCM-41 (PN_xD_y) for the degradation of RhB. The results are shown in Figure 9.

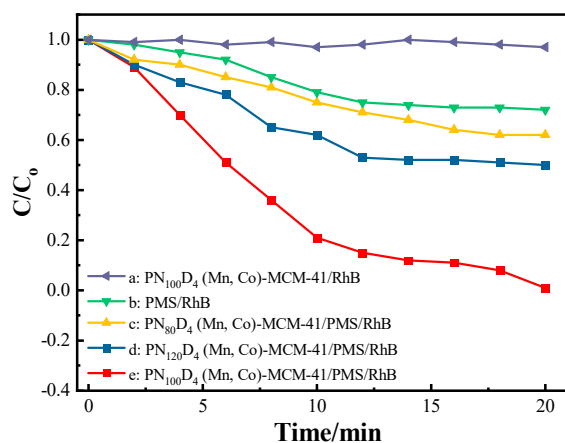


Figure 9. Effect comparison of different catalysts activating PMS to degrade RhB.

RhB was not degraded even with the catalyst when PMS was not added (Figure 9a). The reaction system degraded RhB by 20% with PMS and without Mn-Co-MCM-41 (Figure 9b). This showed that PMS had oxidative properties. However, it could not generate free radicals with strong catalytic activity without a catalyst [35], resulting in poor degradation of RhB. The catalytic effects were all enhanced by adding thermosensitive template agents (Figure 9c–e). The performance of Mn-Co-MCM-41 was slightly enhanced when PN₈₀D₄ was used as the templating agent. The catalytic material's performance was further improved when the hydrophilic ratio increased to PN₁₂₀D₄. However, the material's performance was poor due to the inappropriate hydrophilicity ratio of the templating agent. Until the thermosensitive material PN₁₀₀D₄ was used, the RhB degradation efficiency was close to 100% with the catalytic reaction within 20 min (Figure 9e), while the Co-Fe-MCM-41-type catalyst could reach 100% degradation for a longer time with

60 min [17]. This exciting result is significantly better than that reported in the existing literature [36–38]. It showed that the pore material Mn-Co-MCM-41 (PN₁₀₀D₄) with uniform morphology and size acted as a catalyst in the degradation of RhB. Its catalytic mechanism was that Mn-Co-MCM-41 activated the PMS to the more oxidizing $\text{SO}_4^{\cdot -}$, facilitating the degradation reaction of RhB easier. Thus, the degradation efficiency was improved [39].

3.3.2. Influence of PMS Concentration

The effect of the catalytic reaction on RhB degradation at different PMS concentrations (0, 0.1 mmol/L, 0.2 mmol/L, and 0.3 mmol/L) is shown in Figure 10.

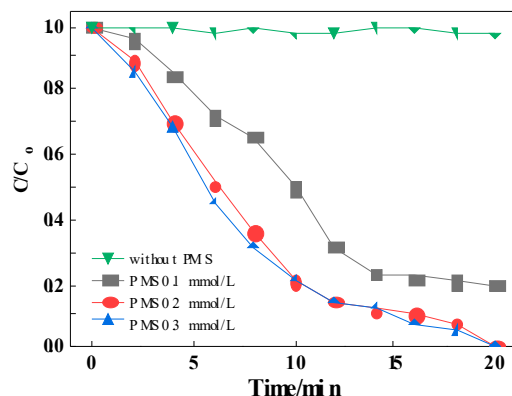


Figure 10. Effect of RhB degradation by PMS at different PMS concentrations.

When using Mn-Co-MCM-41 (PN₁₀₀D₄) as the catalyst, RhB was not degraded even when the catalyst was added without PMS. The degree of RhB degradation increased gradually with increasing PMS concentration. In the system with different concentrations of PMS, the degree of RhB degradation increased by 78%, 100%, and 100%, compared with the system without PMS. It showed that RhB degradation was better when the content of strong oxidizing $\text{SO}_4^{\cdot -}$ in the reaction system was higher. This was due to the increase in the active HSO_5^- in the reaction system by increasing the concentration of PMS, which catalyzed the formation of the strong oxidizing $\text{SO}_4^{\cdot -}$ on the active site of the Mn-Co-MCM-41 (PN₁₀₀D₄) surface. Thus, the degradation efficiency was significantly improved. In this study, a 0.20 mmol/L PMS concentration was finally selected as the optimal PMS dosage for the degradation of RhB. Just as the literature report, with the increase in PMS concentration (0.02–0.06 mM), the degradation of RhB gradually increased. However, when the PMS concentration was further increased, the degradation did not significantly increase [40,41].

3.3.3. Reaction Mechanism of Mn-Co-MCM-41(PN₁₀₀D₄)-Activated PMS for RhB Degradation

It has been reported that ethanol can trap $\cdot\text{OH}$ and $\text{SO}_4^{\cdot -}$ in solution and that isopropanol can trap $\cdot\text{OH}$ in solution [42–44]. Therefore, experiments were designed to verify whether $\cdot\text{OH}$ and $\text{SO}_4^{\cdot -}$ were produced during the reaction. The degradation efficiency of Mn-Co-MCM-41(PN₁₀₀D₄) decreased when isopropanol was added to the reaction system. In addition, the inhibition was more significant when ethanol was added (Figure 11). The results demonstrated that $\text{SO}_4^{\cdot -}$ played an essential role in activating Mn-Co-MCM-41(PN₁₀₀D₄) in the degradation of RhB by PMS. In addition, $\cdot\text{OH}$ was also involved in the degradation process.

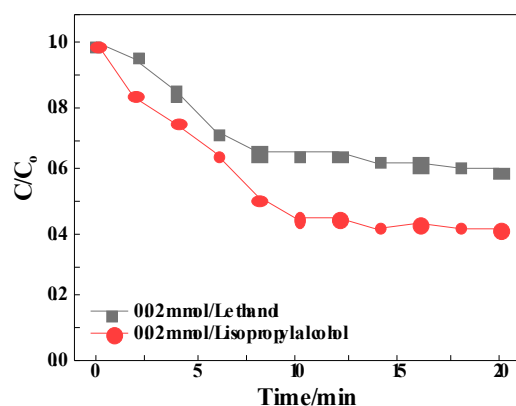


Figure 11. Free radical quenching experiments of the activated PMS degradation RhB reaction system.

Comparative experiments were designed to verify whether oxygen is necessary for the reaction process. Mn-Co-MCM-41(PN₁₀₀D₄) was selected as the catalyst for the RhB degradation experiments by PMS under air and nitrogen atmosphere. The results are shown in Figure 12. It can be seen that the degradation effect under the air atmosphere was significantly higher than that of the nitrogen atmosphere. This was due to the participation of oxygen in the degradation reaction whereby O₂ was reduced to O₂^{•−}. Thus, PMS was activated to produce more SO₄^{•−}, which increased the RhB degradation efficiency [45]. The results showed that SO₄^{•−} could improve the reaction efficiency, and O₂^{•−} also played a crucial role in the Mn-Co-MCM-41(PN₁₀₀D₄)-activated PMS degradation RhB reaction system.

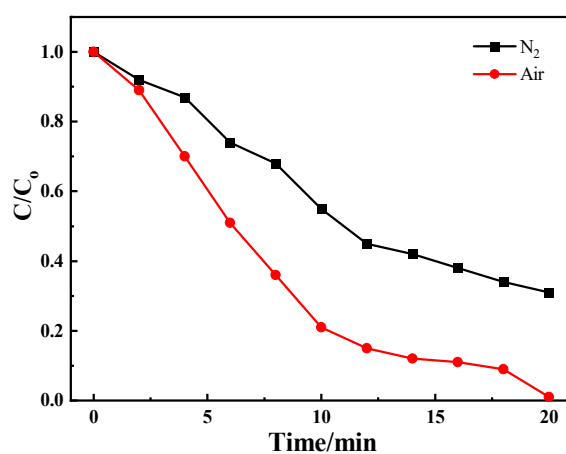


Figure 12. Effect of Mn-Co-MCM-41 (PN₁₀₀D₄) activation of PMS for RhB degradation under different atmospheres.

Based on the above analysis, the reaction mechanism of this experiment was described in Figure 13. The bimetallic Mn-Co-MCM-41(PN₁₀₀D₄) catalyst first reacted with PMS in solution to produce the active species SO₄^{•−} and Co²⁺. The SO₄^{•−} came into contact with H₂O/OH[−] to further produce •OH and also reacted with molecular oxygen adsorbed on the surface of Mn-Co-MCM-41(PN₁₀₀D₄) to release O₂^{•−}. In addition, the three reactive groups simultaneously degraded RhB. As the reaction progressed, Co²⁺ in the solution reacted with PMS to produce SO₄^{•−} and Co³⁺. Then, Co³⁺ reacted with Mn-Co-MCM-41(PN₁₀₀D₄) to produce Co²⁺. Finally, the generated Co²⁺ reacted further with PMS to achieve a cyclic process to achieve the catalytic effect.

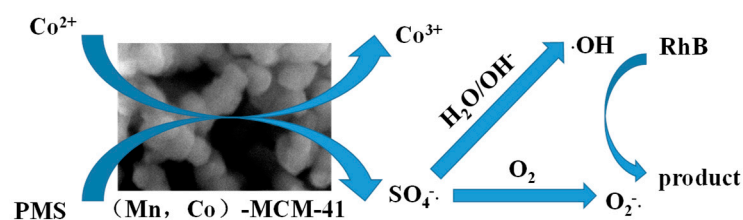


Figure 13. Possible reaction mechanism for the degradation of rhodamine B by Mn-Co-MCM-41.

3.4. Catalyst Recycling Performance

The used catalysts were centrifuged, washed, and dried for the subsequent catalytic reaction. The results showed that the Mn-Co-MCM-41(PN₁₀₀D₄) catalyst was still more than 90% efficient in degrading RhB after six cycles (Figure 14), indicating that the catalyst structure was stable and there was no significant metal loss from the bimetallic loading. To date, many kinds of catalysts can be reused. However, they usually required complex recycling procedures with lower degradation rates [46–48]. In this work, the new Mn-Co-MCM-41(PN_xD_y) catalyst can easily be recycled and run more than six times.

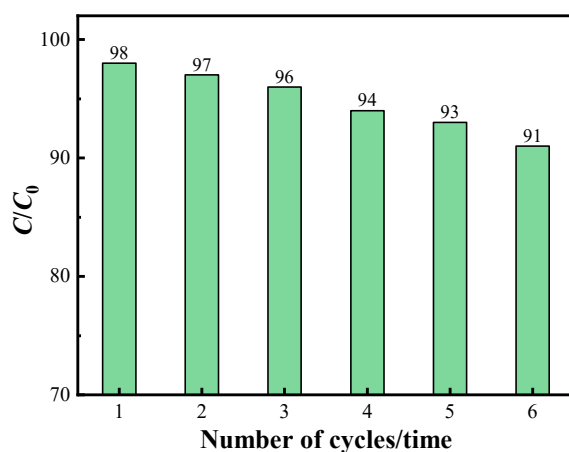


Figure 14. Recycling efficiency of Mn-Co-MCM-41.

4. Conclusions

Bi-metallically Mn and Co doped MCM-41 materials with excellent morphology and properties were prepared by the microwave-assisted hydrothermal method using self-made thermosensitive PN_xD_y as a templating agent. The morphology, structural composition, and thermal stability of the bimetallic-doped MCM-41 molecular sieve were investigated by FTIR, small-angle XRD, SEM, and N₂ adsorption–desorption characterization. We systematically investigated the effects of each condition on the structure and properties of the Mn-Co-MCM-41 molecular sieve. The results showed that:

- The Mn-Co-MCM-41 molecular sieves obtained by bimetallic doping with the 12 hermos-sensitive templating PN₁₀₀D₄ had uniform pore channels and regular morphology.
- Bimetallic (Mn-Co) doping did not destroy the skeletal structure of MCM-41.
- The MCM-41 molecular sieve was loaded with bimetallic (Mn-Co) doping using the thermosensitive polymer material PN₁₀₀D₄ as a templating agent to better activate PMS for RhB degradation. The degradation rate of RhB could reach 98% with a 20 min reaction by Mn-Co-MCM-41 (PN₁₀₀D₄).
- This type of catalyst can be conveniently recycled and recovered for efficient reuse, which is expected to realize industrial applications.

Author Contributions: Conceptualization and funding acquisition, Y.Z.; methodology, data curation and writing, W.P.; formal analysis, Y.L.; writing—review and editing, L.C. All authors have read and agreed to the published version of the manuscript.

Funding: This research was funded by the National Natural Science Foundation of China (22278118; 22108065) and the Postgraduate Scientific Research Innovation Project of Hunan Province (QL20220189).

Institutional Review Board Statement: Not applicable.

Data Availability Statement: The data presented in this study are available from the corresponding author upon request.

Conflicts of Interest: The authors declare no conflict of interest.

References

1. Nandigana, P.; Mahato, S.; Dhandapani, M.; Pradhan, B.; Subramanian, B.; Panda, S.K. Lyophilized tin-doped MoS₂ as an efficient photocatalyst for overall degradation of Rhodamine B dye. *J. Alloys Compd.* **2022**, *907*, 164470. [[CrossRef](#)]
2. Li, Z.; Zhang, X.; Lin, J.; Han, S.; Lei, L. Azo dye treatment with simultaneous electricity production in an anaerobic-aerobic sequential reactor and microbial fuel cell coupled system. *Bioresour. Technol.* **2010**, *101*, 4440–4445. [[CrossRef](#)] [[PubMed](#)]
3. Olaru, P. Synthesis and testing of cellulose acetate nicotinate as adsorbent for rhodamine B dye. *J. Appl. Polym. Sci.* **2019**, *136*, 47772. [[CrossRef](#)]
4. Saeed, M.; Ahmad, A.; Boddula, R.; Inamuddin; Haq, A.U.; Azhar, A. Ag@Mn_xO_y: An effective catalyst for photo-degradation of rhodamine B dye. *Env. Chem. Lett.* **2017**, *16*, 287–294. [[CrossRef](#)]
5. Singh, S.; Parveen, N.; Gupta, H. Adsorptive decontamination of rhodamine-B from water using banana peel powder: A biosorbent. *Environ. Technol. Innov.* **2018**, *12*, 189–195. [[CrossRef](#)]
6. Hira, S.A.; Yusuf, M.; Annas, D.; Hui, H.S.; Park, K.H. Biomass-derived activated carbon as a catalyst for the effective degradation of rhodamine B dye. *Processes* **2020**, *8*, 926. [[CrossRef](#)]
7. Gunnagol, R.M.; Rabinal, M. TiO₂-graphene nanocomposites for effective photocatalytic degradation of rhodamine-B dye. *Chemistryselect* **2018**, *3*, 2578–2585. [[CrossRef](#)]
8. Moghaddam, S.S.; Moghaddam, M.R.A.; Arami, M. Coagulation/flocculation process for dye removal using sludge from water treatment plant: Optimization through response surface methodology. *J. Hazard. Mater.* **2010**, *175*, 651–657. [[CrossRef](#)]
9. Gupta, H. Photocatalytic degradation of phenanthrene in the presence of akaganeite nano-rods and the identification of degradation products. *Rsc. Adv.* **2016**, *6*, 112721–112727. [[CrossRef](#)]
10. Mishra, S.; Maiti, A. The efficiency of Eichhornia crassipes in the removal of organic and inorganic pollutants from wastewater: A review. *Environ. Sci. Pollut. Res. Int.* **2017**, *24*, 7921–7937. [[CrossRef](#)]
11. Ai, X. Ag/AgCl-GO: A composite for degradation of Rhodamine B in dye wastewater. *Adv. Powder Technol. Int. J. Soc. Powder Technol. Jpn.* **2019**, *30*, 3193–3202. [[CrossRef](#)]
12. Sachdeva, S.; Kumar, A. Preparation of nanoporous composite carbon membrane for separation of rhodamine B dye. *J. Membr. Sci.* **2009**, *329*, 2–10. [[CrossRef](#)]
13. Yasin, M.; Saeed, M.; Muneer, M.; Usman, M.; Ul, H.A.; Sadia, M.; Altaf, M. Development of Bi₂O₃-ZnO heterostructure for enhanced photodegradation of rhodamine B and reactive yellow dyes. *Surf. Interfaces* **2022**, *30*, 101846. [[CrossRef](#)]
14. AbdulRazak, A.A.; Rohani, S. Sodium dodecyl sulfate-modified Fe₂O₃/molecular sieves for removal of rhodamine B dyes. *Adv. Mater. Sci. Eng.* **2018**, *2018*, 3849867. [[CrossRef](#)]
15. Chen, B.; Hui, B.; Dong, Y.; Sheng, Q.; Li, X.; Hao, Q.; Liu, C. Distributions of Ni in MCM-41 for the hydrogenation of N-ethylcarbazole. *Fuel* **2022**, *324*, 124405. [[CrossRef](#)]
16. Gao, Y.; Chen, H.; Tay-Agbozo, S.; Kispert, L.D. Photo-induced electron transfer of carotenoids in mesoporous sieves (MCM-41) and surface modified MCM-41: The role of hydrogen bonds on the electron transfer. *J. Photochem. Photobiol. A Chem.* **2017**, *341*, 1–11. [[CrossRef](#)]
17. Lin, K.A.; Chen, B.; Chen, C. Evaluating Prussian blue analogues M^{II}₃[M^{III}(CN)₆]₂ (MII=Co, Cu, Fe, Mn, Ni; MIII=Co, Fe) as activators for peroxymonosulfate in water. *Rsc. Adv.* **2016**, *6*, 92923–92933. [[CrossRef](#)]
18. Zhai, Q. Study on SBA-15 as an effective sorbent for dye butyl rhodamine B. *J. Sol-Gel Sci. Technol.* **2020**, *96*, 34–46. [[CrossRef](#)]
19. Albayati, T.M.; Alwan, G.M.; Mahdy, O.S. High performance methyl orange capture on magnetic nanoporous MCM-41 prepared by incipient wetness impregnation method. *Korean J. Chem. Eng.* **2017**, *34*, 259–265. [[CrossRef](#)]
20. Sar, Y.; Lmaz, M.; Dere Zdemir, Z.; Pi Kin, S. Synthesis and characterization of MCM-41 with different methods and adsorption of Sr²⁺ on MCM-41. *Res. Chem. Intermediat.* **2013**, *41*, 199–211.
21. Selvaraj, M.; Pandurangan, A.; Seshadri, K.S.; Sinha, P.K.; Lal, K.B. Synthesis, characterization and catalytic application of MCM-41 mesoporous molecular sieves containing Zn and Al. *Appl. Catal. A Gen.* **2003**, *242*, 347–364. [[CrossRef](#)]

22. Huang, W.; Liu, J.; Rao, N.; Fan, G.; Yan, J.; Cheng, Q.; Song, G. Influence of surfactant on CO₂ adsorption of amine-functionalized MCM-41. *Env. Technol.* **2021**, *43*, 4545–4553. [[CrossRef](#)] [[PubMed](#)]
23. Fernandes, G.J.T.; Coriolano, A.C.F.; Silva, J.B.; Castro, F.L.; Fernandes, V.J.; Araujo, A.S. Synthesis characterization and acid properties of niobium-containing MCM-41. *J. Therm. Anal. Calorim.* **2018**, *131*, 691–695. [[CrossRef](#)]
24. Kaur, T.S.; Prakash, K.J.; Kumar, S.V. Adsorptive interaction of 4-aminobiphenyl with mesoporous MCM-41. *Phys. Chem. Liq.* **2018**, *57*, 720–732.
25. Molaei, S.; Tamoradi, T.; Ghadermazi, M.; Ghorbani-Choghamarani, A. Highly Efficient Oxidative Coupling of Thiols and Oxidation of Sulfides in the Presence of MCM-41@Tryptophan-Cd and MCM-41@Tryptophan-Hg as Novel and Recoverable Nanocatalysts. *Catal. Lett.* **2018**, *148*, 1834–1847. [[CrossRef](#)]
26. Hagio, T.J.Y.Y. Facile Hydrothermal Synthesis of EAB-Type Zeolite under Static Synthesis Conditions. *Cryst. Res. Technol. J. Exp. Ind. Crystallogr.* **2021**, *56*, 2000163. [[CrossRef](#)]
27. Pradhan, A.; Sahoo, M.; Bellamkonda, S.; Parida, K.M.; Rao, G.R. Enhanced photodegradation of dyes and mixed dyes by heterogeneous mesoporous Co-Fe/Al₂O₃-MCM-41 nanocomposites: Nanoparticles formation, semiconductor behavior and mesoporosity. *Rsc. Adv.* **2016**, *6*, 94263–94277. [[CrossRef](#)]
28. Zhang, M.; Yang, J.H. Selective Hydrogenation of Furfural: Pure Silica Supported Metal Catalysts. *Chemistryselect* **2022**, *7*, e202200013. [[CrossRef](#)]
29. Zhao, Y.; Wang, H.; Ji, J.; Li, X.; Yuan, X.; Duan, A.; Guan, X.; Jiang, L.; Li, Y. Recycling of waste power lithium-ion batteries to prepare nickel/cobalt/manganese-containing catalysts with inter-valence cobalt/manganese synergistic effect for peroxymonosulfate activation. *J. Colloid. Interf. Sci.* **2022**, *626*, 564–580. [[CrossRef](#)]
30. Zhang, Y.; Tan, R.; Zhao, G.; Luo, X.; Xing, C.; Yin, D. Thermo-responsive self-assembled metallomicelles accelerate asymmetric sulfoxidation in water. *J. Catal.* **2016**, *335*, 62–71. [[CrossRef](#)]
31. Ramallo-López, J.M.; Ledesma, E.J.; Requejo, F.G.; Rodríguez, J.A.; Kim, J.; Rosas-Salas, R.; Domínguez, J.M. XANES Characterization of Extremely Nanosized Metal-Carbonyl Subspecies (Me = Cr, Mn, Fe, and Co) Confined into the Mesopores of MCM-41 Materials. *J. Phys. Chem. B* **2004**, *108*, 20005–20010. [[CrossRef](#)]
32. Yu, H.; Ding, D.; Zhao, S.; Faheem, M.; Mao, W.; Yang, L.; Chen, L.; Cai, T. Co/N co-doped porous carbon as a catalyst for the degradation of RhB by efficient activation of peroxymonosulfate. *Env. Sci. Pollut. R* **2023**, *30*, 10969–10981. [[CrossRef](#)]
33. Liu, J.; Sui, H.; Sheng, L. Hydrothermal synthesis, characterization and catalytic performance of Mn-MCM-41 mesoporous molecular sieve. *Mod. Chem. Ind.* **2018**, *38*, 93–97.
34. Kong, Y.; Zhu, H.; Yang, G.; Guo, X.; Hou, W.; Yan, Q.; Gu, M.; Hu, C. Investigation of the structure of MCM-41 samples with a high copper content. *Adv. Funct. Mater.* **2004**, *14*, 816–820. [[CrossRef](#)]
35. Zhou, H.; Zhu, X.; Chen, B. Magnetic biochar supported α -MnO₂ nanorod for adsorption enhanced degradation of 4-chlorophenol via activation of peroxydisulfate. *Sci. Total Env.* **2020**, *724*, 138278. [[CrossRef](#)]
36. Masteri-Farahani, M.; Mosleh, N. CdS quantum dots encapsulated within the mesopores of MCM-41 and interlayers of montmorillonite as photocatalysts for rhodamine-B degradation in aqueous solution. *Env. Sci. Pollut. R* **2021**, *28*, 4615–4622. [[CrossRef](#)]
37. Zhao, C.; Cai, L.; Wang, K.; Li, B.; Yuan, S.; Zeng, Z.; Zhao, L.; Wu, Y.; He, Y. Novel Bi₂WO₆/ZnSnO₃ heterojunction for the ultrasonic-vibration-driven piezocatalytic degradation of RhB. *Env. Pollut.* **2023**, *319*, 120982. [[CrossRef](#)]
38. Cui, Z.; Wu, H.; Bai, K.; Chen, X.; Li, E.; Shen, Y.; Wang, M. Fabrication of a g-C₃N₄/MoS₂ photocatalyst for enhanced RhB degradation. *Phys. E Low-Dimens. Syst. Nanostruct.* **2022**, *144*, 115361. [[CrossRef](#)]
39. Zhu, W.; Wang, H.; Liu, W. The characteristics of degradation of rhodamine B by quinone-activated persulfate process. *China Environ. Sci.* **2016**, *36*, 1732–1737.
40. Chen, X.; Liu, L. PMS activation over MoS₂/Co_{0.75}Mo₃S_{3.75} for RhB pollutant oxidation removal in fuel cell system. *J. Environ. Chem. Eng.* **2022**, *10*, 107449. [[CrossRef](#)]
41. Liu, C.; Pan, D.; Tang, X.; Hou, M.; Zhou, Q.; Zhou, J. Degradation of Rhodamine B by the α -MnO₂/Peroxymonosulfate System. *Water Air Soil Pollut.* **2016**, *227*, 92. [[CrossRef](#)]
42. Anipsitakis, G.P.; Dionysiou, D.D. Degradation of organic contaminants in water with sulfate radicals generated by the conjunction of peroxymonosulfate with cobalt. *Env. Sci. Technol.* **2003**, *37*, 4790–4797. [[CrossRef](#)] [[PubMed](#)]
43. Di, S.; Wang, J.; Zhai, Y.; Chen, P.; Ning, T.; Shi, C.; Yang, H.; Bao, Y.; Gao, Q.; Zhu, S. Efficient activation of peroxymonosulfate mediated by Co(II)-CeO₂ as a novel heterogeneous catalyst for the degradation of refractory organic contaminants: Degradation pathway, mechanism and toxicity assessment. *J. Hazard. Mater.* **2022**, *435*, 129013. [[CrossRef](#)] [[PubMed](#)]
44. Duan, L.; Yin, S.; Li, M.; Kang, X.; Wu, Z.; Zhao, S.; Liao, F. The synthesis of dandelion-like CuO nanoflowers and photocatalytic degradation of RhB. *Colloid. Polym. Sci.* **2017**, *295*, 1797–1803. [[CrossRef](#)]
45. Shimizu, A.; Tokumura, M.; Nakajima, K.; Kawase, Y. Phenol removal using zero-valent iron powder in the presence of dissolved oxygen: Roles of decomposition by the Fenton reaction and adsorption/precipitation. *J. Hazard. Mater.* **2012**, *201–202*, 60–67. [[CrossRef](#)] [[PubMed](#)]
46. Kianfar, A.H.; Arayesh, M.A.; Momeni, M.M. Degradation of MB and RhB by modified ZrO₂ nanoparticles via sunlight. *Appl. Phys. A* **2021**, *127*, 158. [[CrossRef](#)]

47. Frindy, S.; Sillanpää, M. Synthesis and application of novel α -Fe₂O₃/graphene for visible-light enhanced photocatalytic degradation of RhB. *Mater. Des.* **2020**, *188*, 108461. [[CrossRef](#)]
48. Liu, P.; Xing, L.; Lin, H.; Wang, H.; Zhou, Z.; Su, Z. Construction of porous covalent organic polymer as photocatalysts for RhB degradation under visible light. *Sci. Bull.* **2017**, *62*, 931–937. [[CrossRef](#)]

Disclaimer/Publisher's Note: The statements, opinions and data contained in all publications are solely those of the individual author(s) and contributor(s) and not of MDPI and/or the editor(s). MDPI and/or the editor(s) disclaim responsibility for any injury to people or property resulting from any ideas, methods, instructions or products referred to in the content.